A New Functional Composite for Photovoltaic and Sensor Applications

Puja Ghosh[a], Anurag Roy[a,b], Soumita Mukhopadhyay[a], Mousumi Narjinary[a], Senthilarasu Sundaram[b], Shrabanee Sen[a] and Parukuttyamma Sujatha Devi[a,c,*]

[a]Functional Materials and Devices Division, CSIR-Central Glass and Ceramic Research Institute, Jadavpur, Kolkata 700032, India

[b]Environment and Sustainability Institute, University of Exeter, Penryn Campus, Cornwall TR10 9FE, U.K.

[c]Chemical Sciences and Technology Division, CSIR-National Institute of Interdisciplinary Science and Technology, Thiruvananthapuram 695019, India

Abstract

As a preliminary drive to eventually develop dye-sensitized solar cell (DSSC)-powered gas sensors, many oxide-based systems have been explored to fabricate sensors that can show response at room temperature for any analyte gas. As an outcome of recent work in this endeavor, a composite nanorod of anatase TiO_2 with $Na_{0.23}TiO_2$ is found to exhibit both photovoltaic performance and gas sensing at room temperature as demonstrated here. An interesting morphology change along with a phase change from nanoparticle to nanorod is observed during the hydrothermal synthesis of anatase TiO_2 nanoparticles with sodium hydroxide under a highly basic condition. In order to understand the effect of the minor phase $Na_{0.23}TiO_2$ on the inherent properties of anatase TiO_2, the application of nanorod composite in two unique potential application areas, DSSC and acetone sensings is investigated. The composite material exhibits an enhanced efficiency of 7.85% for a DSSC. Surprisingly, a resistive sensor fabricated with the synthesized composite material exhibits room temperature p-type sensing behavior toward different concentrations of acetone (10, 5, 3, 2, and 1 ppm) with high selectivity.

1. Introduction

TiO_2 has been known to exist mainly in three primary crystallographic modifications such as anatase (tetragonal), rutile (tetragonal) and brookite (orthorhombic) forms at ambient conditions. During the past few decades, the above mentioned TiO_2 polymorphs have been widely investigated for diverse applications due to their well accepted electronic and optical properties.[1,2] For example, as a photocatalyst for environmental applications, anatase is more preferred than rutile due to its inherent optoelectronic properties.[3-5] There has been many efforts to improve the optoelectronic properties of titania and an effective way of further modifying the electronic properties of TiO_2 is doping, though ion-implant, shape control and surface modifications are also being explored to improve the properties of TiO_2. In DSSCs, the anatase phase is considered to be the best suited material so far exhibiting higher photovoltaic performance than other polymorphs of TiO_2.[6-8] In order to enhance the performance and related efficiency of DSSC, significant efforts have been devoted in improving the host TiO_2, which acts as a framework for DSSCs. However, mixing different phases followed by a hetero-structure formation of TiO_2 has been found to result in better power-conversion efficiency (PCE) than the sole usage of pure anatase. The hetero-structure and mixed-phase formation could directly affect the charge transfer process between the different phases, possibly by reducing the recombination of photogenerated electrons and enhancing the electron mobility. In many cases, the synergistic effects of the three factors, such as electron transfer efficiency, light scattering and dye adsorption together leading to higher current density (J_{SC}) have been reported.[9,10] In order to improve the efficiency of TiO_2, one-dimensional nanostructures of TiO_2, such as nanorods, nanotubes and nanowires, have also been studied [11,12] which are expected to significantly improve the electron transport properties due to directionally smooth electron mobility and lower inter-crystalline contacts.[13-16] As reported by others, $Na_{0.23}TiO_2$ with a monoclinic crystal structure is expected to form a p-n junction with TiO_2 which allows faster electron-hole separation followed by mobility via synergistic effect.[17,18] Wang et al. (2018) reported $TiO_2/Na_{0.23}TiO_2$ as a heterojunction photocatalyst helpful for the photogenerated electron-hole pairs separation, resulting in an enhanced photocatalysis.[19] The same group also reported an effective method to prove the surface plasmon property of a composite directly and highlighted the application of $Na_{0.23}TiO_2$ in photocatalysis.[20] Recently, understanding the influence of synthesis parameters on the structure, morphology, and properties of titanate nanorods derived by NaOH treatment of TiO_2 nanoparticles has been reported by Silva et al., (2019).[21] There are also reports confirming the lower photocatalytic activity of TiO_2-coated soda-lime glass than that of the TiO_2-coated quartz due to the diffusion of Na^+ into the TiO_2 film from the soda-lime glass substrate.[22,23] However, there are only very few reports on the effect of Na^+ on the photovoltaic properties of TiO_2 materials in DSSCs. The photovoltaic properties of NaOH-washed anatase TiO_2 nanosheets with exposed {0 0 1} facets were also investigated for DSSC. [24] The effect of sodium doping in improving the performance of DSSC was reported by Shalini et al. (2018). They recorded a PCE of 6% for sodium doped TiO_2.[25]] It is worth mentioning that only very few reports are available on $Na_{0.23}TiO_2/TiO_2$ nanorods for DSSC application.

Recently, we have reported the performance of Au decorated ZnO/TiO_2 as a stable photocatalyst and TiO_2-polyaniline composite as a photoanode in dye-sensitized solar cells.[26,27] In addition, as a preliminary effort to eventually develop DSSC powered gas sensor, we have been exploring many oxide based systems to fabricate sensors that could exhibit response at room temperature for any analyte gas. As an outcome of our recent work in this endeavor, a composite nanorod (CR) of anatase TiO_2 with $Na_{0.23}TiO_2$ has been found to exhibit both photovolatic performance and gas sensing at room temperature as demonstrated in this work. Thus, in this article, we report the synthesis of TiO_2 anatase-$Na_{0.23}TiO_2$ composite nanorod by a hydrothermal synthesis using sodium hydroxide (NaOH) and its dual functional application in DSSC and sensing. We investigated the formation of $Na_{0.23}TiO_2$ nanorod and its influence and performance on TiO_2 anatase photoanode in DSSC. In addition, the synthesized composite nanorod has also been explored for gas sensing applications. An enhanced p-type semiconducting sensing response was achieved for different concentrations of acetone (10, 5, 3, 2 and 1 ppm) along with strong selectivity and reproducibility towards acetone at room temperature.

2. Results and Discussion

2.1. Thermal Analysis

The thermal decomposition nature of the prepared sample at pH 12 is shown in Figure S1, ESI, which exhibited an overall weight loss of ~9% within the temperature range of room temperature to 550°C. Initially, about 3% weight change was observed between 30 and 180ºC followed by a small weight change at 400 ºC corresponding to the removal of water in the as-prepared powder sample. Finally, the weight loss became almost negligible above 400°C. The corresponding DTA curve exhibited a broad exothermic change in the range of 150-400°C, indicating crystallization of the as-prepared powder sample. Based on the information observed from the TG-DTA analysis, the as-prepared powder was calcined at 500°C to receive the phase pure final compound.

2.2. Effect of pH on Phase Change and Morphology

The effects of pH during the synthesis and its effect on the phase transformation were investigated through systematic analysis of the data collected from powder X-ray diffraction (XRD) and Field effect scanning electron microscopy (FESEM) (Figure 1). Figure 1a depicts the XRD patterns of starting TiO_2 powder and as prepared powder at pH 8, 10 12 and 14, using NaOH, under identical conditions. The XRD pattern of the starting commercial TiO_2 powder confirmed it to be the anatase phase of TiO_2 only (JCPDS No. 21-1272). During the reaction the same phase is retained up to pH 10. There is an indication of a second phase, $Na_{0.23}TiO_2$ at pH 12. The observed reflections of the new phase matched well with the monoclinic $Na_{0.23}TiO_2$ phase (JCPDS No. 22-1404). Thus, the final resultant product obtained from the hydrothermal treatment of commercial TiO_2 anatase nanoparticle powder exhibits mainly anatase TiO_2 phase with a minor amount of $Na_{0.23}TiO_2$ as a co-existed phase.

The growth of this phase continues at a higher pH of ~14 also.

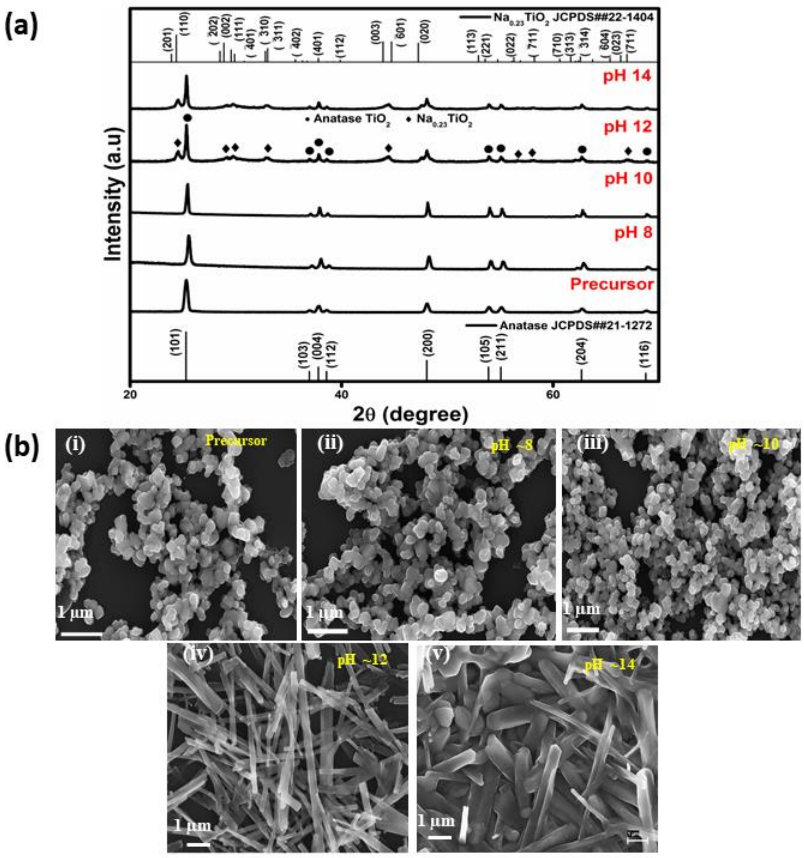

Figure 1. (a) The XRD patterns of synthesized products obtained after hydrothermal treatment of anatase TiO_2 nanoparticle at different pH and (b) FESEM microstructural images of precursor powder and hydrothermally prepared samples at different pH from 8 to 14.

Therefore, pH 12 has been fixed as the optimum condition to form $Na_{0.23}TiO_2$ phase along with the anatase phase. Systematic microstructural analysis was also performed to understand the effect of pH if any on the morphology of the starting material. A change in the morphology of the starting material started to appear with change in pH, and a distinct change in morphology was observed at pH 12. The topotactic transformation of particles and the formation of rod-shaped material is apparent in Figure 1b. Further, at higher pH (~14), the rods get fused as shown in Figure 1b(v) probably due to the extreme basic condition. Thus, it is evident from Figure 1b that the starting anatase particles have transformed to rods during the hydrothermal reaction in presence of NaOH and further annealing at 500^{o}C. Thus, based on the TG-DTA and XRD results, the 500^{o}C calcined sample was selected for further studies.

2.3. Optimization of Hydrothermal Conditions

In order to further evaluate the effect of hydrothermal reaction duration on the above observed changes, which led to the formation of anatase/$Na_{0.23}TiO_2$ co-existed nanorods the duration of the experimental conditions have been varied from 8h to 48 h. After optimizing the pH at 12, where a change in shape was noticed as shown in Figure 1, we varied the duration of the reaction at pH 12. The observed change in structure during this variation is shown in Figure 2. It is clear from Figure 2 the importance of hydrothermal reaction duration on the phase formation and morphological changes of the resulting products, where a change in morphology from particles to rods along with a structural change was noticed. Such a change was evident on increasing the hydrothermal reaction at pH 12 and 180^{o}C to 48h at as shown in Figure 2. As observed from the XRD analysis, the anatase phase was retained up to 12 h of hydrothermal treatment, beyond which it transformed to a mixed phase of anatase and $Na_{0.23}TiO_2$ by 36 h. Finally, the compound formed after 48 h of hydrothermal treatment at 180^{o}C temperature was a rod shaped composite of anatase TiO_2 with $Na_{0.23}TiO_2$. The increase of the hydrothermal reaction time to 48 h led to only a minor increase in surface area of the product along with complete crystallization of the titanate phase.

In order to monitor the structural changes if any during the phase transformation, we have also taken successive FESEM images of the samples as shown in Figure 2. The precursor anatase TiO_2 which was in the particle form successively transformed into nanorod on increasing the hydrothermal reaction duration from 12 to 48 h.

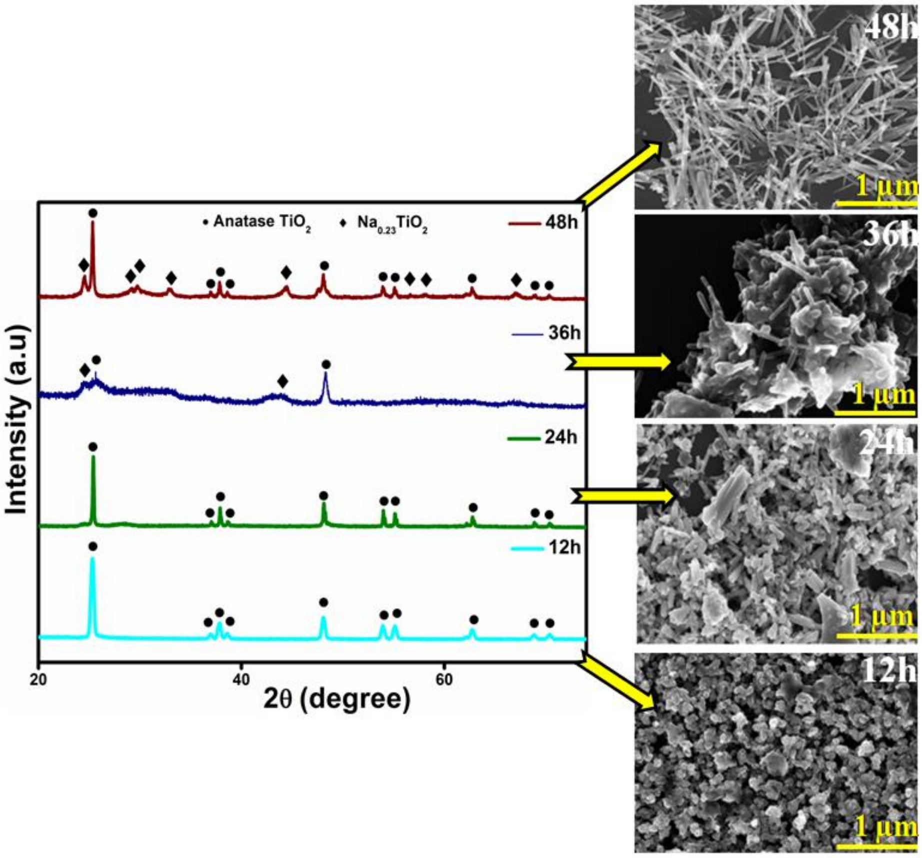

Figure 2. The X-ray diffraction patterns along with the respective FESEM pictures of the hydrothermally prepared samples at a temperature of 180°C for different durations of the reaction.

This structural transformation could have happened by Ostwald ripening during which many small crystals slowly disappear, except for a few that grow larger at the expense of the small crystals, which act as fuel for the growth of bigger crystals. [29,30] Kolen'ko et al. (2006) reported the synthesis of nanorods in one step by hydrothermal treatment in a NaOH solution followed by an acid treatment to produce Na-free nanorods.[30] By following a similar type of acid wash process, we also could generate sodium-free samples. Acid treatment was found to be essential in removing excess sodium to obtain sodium-free nanorods. To qualitative analyze the presence of chloride ion in the sample after acid washing, a small amount of the composite sample was treated with 0.1M aqueous $AgNO_3$ solution, where no white precipitate was formed indicating the absence of chloride ion and NaCl in the sample solution. Thus, successive acid washing and subsequent test with $AgNO_3$ helped in getting sodium ion free composite rod sample.

Figure S2, ESI indicates the effect of acid washing to remove the excess Na from the as-prepared sample, followed by multiple washing with de-ionized water to form the targeted composite product. Initially, the as collected powder sample after the hydrothermal synthesis appeared less crystalline (Figure S2a, ESI). In order to remove the unreacted sodium ion from the precipitated sample, HCl washing was performed, which produced NaCl as a by-product followed by reducing the solution pH to ~7. After HCl wash NaCl phase appeared as the dominating phase (Figure S2b, ESI). However, after thoroughly washing with de-ionized water, excess NaCl also gets completely dissolved, and the synthesized rods exhibited only the mixed-phase with enhanced crystallinity (Figure S2c, ESI). Corresponding EDX analysis of the as-prepared sample, HCl washed sample and de-ionised water washed sample are shown in Figure S3, ESI. This further confirms complete removal of unreacted Na^+ ions and formation of composite powder.

Raman studies were also carried out to further understand the presence of both TiO_2 anatase phase and $Na_{0.23}TiO_2$ in the final product. Figure S4, ESI depicts the characteristic E_g band at 143.4 and 639 cm^{-1}, the B_{1g} band at 397 cm^{-1}, and the (A_{1g} + B_{1g}) mode centred at 516 cm^{-1} of anatase phase of TiO_2. After the hydrothermal treatment, the characteristic E_g mode becomes narrower and slightly blue-shifted from 143.4 to 148 cm^{-1}. This may be due to the phonon-confinement effect developed strain owing to the change in size and shape of TiO_2 during the hydrothermal synthesis process.[31] Also, the weaker Raman bands at 202.4, 285.3 and 449.6

cm^{-1} confirm the presence of sodium titanate phase (NT) in the sample beside the anatase TiO_2.

2.4. Transmission Electron Microscopic (TEM) Analysis

More clear evidence for the formation of nanorod morphology can be found in Figure 3a-i, from the detailed TEM investigation of anatase/$Na_{0.23}TiO_2$ co-existed composite in a single nanorod. Figure 3a,b represents the TEM bright-field image of the precursor TiO_2 nanoparticles at different magnifications confirming an average particle size of 30 nm. The high-resolution TEM (HRTEM) image (Figure 3c) clearly shows an interlayer spacing value of 0.351 nm corresponding to (101) crystal plane of anatase TiO_2 phase. On the other hand, TEM bright-field images of the prepared anatase/$Na_{0.23}TiO_2$ co-existed sample exhibited a rod-like structure having an average diameter of 22 nm, as shown in Figure 3d&e at different magnifications. The corresponding HRTEM shown in Figure 3f indicates the co-existence of (001) plane of $Na_{0.23}TiO_2$ and (101) plane of anatase TiO_2.

Further, the TEM bright-field images of calcined sample exhibit randomly distributed fine thinner rod-like structure having an average diameter of ~10 nm and an aspect ratio of 25:1 as shown in Figure 3g&h at different magnifications. The good crystallinity of the synthesized nanorods is clear from the HRTEM image, as shown in Figure 3i. Further, the interlayer spacing of the most intense (101) peak is found 0.351 nm along with (004) plane (0.237 nm) corresponding to anatase TiO_2 phase, which corroborates with the XRD and Raman analysis.

The colour elemental mapping of the same sample was executed, as shown in Figure S5a, ESI EDX analysis. The extensive area mapping ensures homogeneous distribution of Ti and O, and successful incorporation of Na, as the only element present in the composite nanorods. Besides, the quantitative EDX analysis stipulates an insufficient amount of O in composite nanorods, as shown in Figure S5b, ESI. The atomic percentage of elemental composition indicates ~5.6% of Na availability in the composite nanorod (inset of Figure S5b, ESI).

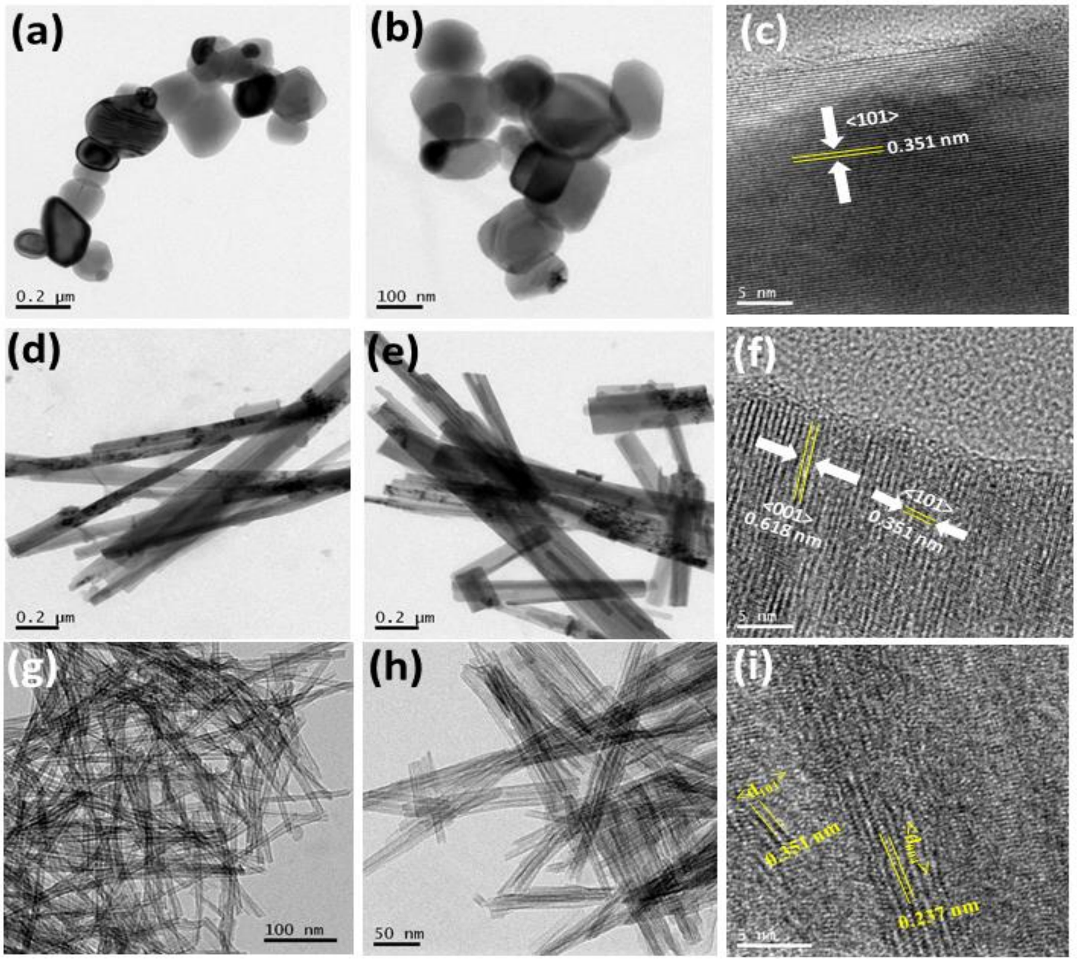

Figure 3. (a)-(b) TEM bright-field images of starting anatase TiO_2 powder at different magnifications, (c) corresponding HRTEM image, (d)-(e) TEM bright-field images at different magnifications and (f) corresponding HRTEM image of the as-prepared nanorod, (g)-(h) TEM bright-field images at different magnifications and (i) corresponding HRTEM image of composite nanorod calcined at 500^{o}C.

As described in other reports, the formation of layered nanosheets might be the initial step for the formation of rods which then become seeds for an oriented crystal growth process leading to thinner titanate nanorods. [32,33] In addition, the period of hydrothermal treatment determines the formation of this 1D morphology.

According to many reports, the phase and morphology transformation during hydrothermal synthesis strongly depended on the NaOH content.[32, 22] The TiO_2 nanoparticles in highly basic medium in NaOH could lead to the formation of lamellar sheets due to the breakage of Ti-O-Ti bonds and form O-Ti, Ti-OH bonding and the loose O-Ti could bind to Na^+ forming Ti-O-Na. The intermediates such as Ti-OH would proceed with rearrangement to form sheets of edge-sharing TiO_6 octahedra with Na^+ and OH^- intercalated between the sheets. These two longer Ti-O bonds in the TiO_6 octahedra were broken, partially the anatase TiO_2 would transform into the layered titanate.[34] The hydrothermal reaction of TiO_2 nanoparticles in high pH condition with NaOH might have helped in the formation of sodium tri-titanate ($Na_2Ti_3O_7$) particles with a rod-like morphology.[35]

For instance, for protonated TiO_2 nanorods, pure anatase phase is usually formed, whereas, for Na^+ rich nanorods, post-annealing leads to a mixed phase. The ion exchange of Na^+ by H^+ is a well-known mechanism reported in the literature. [36,37] The measured zeta potential of the precursor anatase nanoparticle was -49.2 mV, indicating highly water-soluble colloidal solution whereas, in case of the synthesized nanorod, the zeta potential value gets reduced to -12.6 mV.

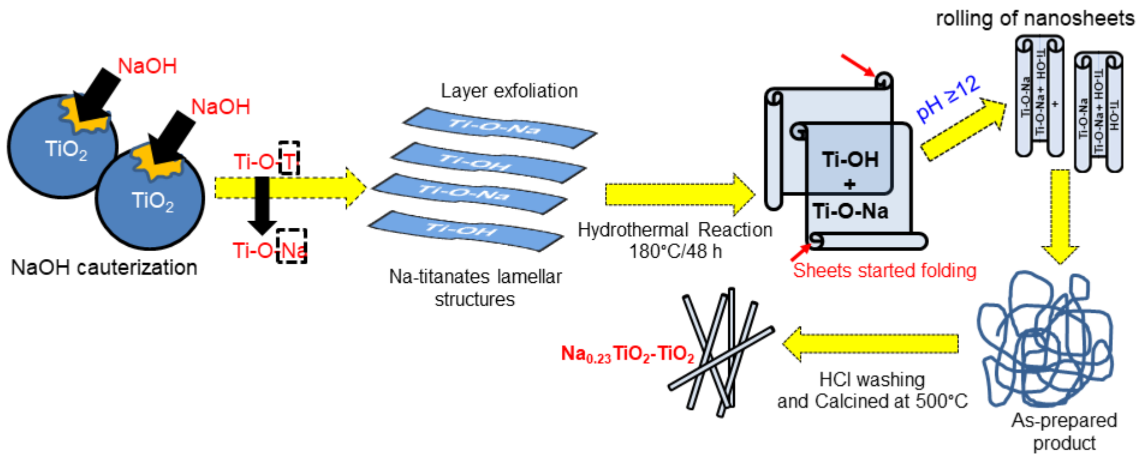

Scheme 1. Schematic representation of the growth mechanism of composite nanorods.

2.7. X-ray Photoelectron Spectroscopic (XPS) Analysis

To understand the chemical and binding states of the elements present in TiO_2 nanoparticle (TP) and composite nanorod (CR), X-ray photoelectron spectroscopy (XPS) studies were carried out as shown in (Figure 4a-e). It is evident that both samples contain Ti and O, as shown in the XPS survey spectra in Figure 4a. The appearance of metallic Na specifies the existence of Na in CR sample. The core-level binding energy peaks at 493.2 and 1070.1 eV indicates Na KLL and Na 1s states, respectively (Figure 4b). The XPS peaks at 464.42eV and 458.62 eV correspond to binding energies of the Ti $2p_{3/2}$ and $2p_{1/2}$ states, respectively of TP sample. The binding energy of CR exhibited a significant stokes shift, i.e. 463.75 and 457.95 eV of the Ti $2p_{3/2}$ and $2p_{1/2}$ states, respectively, as shown in Figure 4c. This may be due to the co-existence of tetragonal-monoclinic phase.[15,38] Besides, the peak shifting sometimes may be attributed to the lower electronegativity of Na (0.93) than that of Ti (1.52), which confirms the substitutional incorporation of Na^+ at Ti^{4+} site.[39] For both the samples, the spin-orbit splitting energy of 5.8 eV is characteristic of Ti^{4+} in the TiO_2 form. At the same time, the O1s binding energy gets decreased for CR than TP. By deconvolution, the observed three peaks of O1s shown in Figure 4d,e represents the high-resolution O1s spectrum of TP and CR samples, respectively. The observed two different binding energies are attributed to Ti-O-Ti for both the samples as O1 component and Ti-O-H as O2 component for both the samples (Figure 4d,e). The oxygen deficiency of CR sample as observed from XPS analysis for O1s spectrum further corroborates the quantitative EDX data (Figure S5b, ESI). Table S1, ESI indicates the individual core level binding energies and their difference for both the samples. Interestingly, TP exhibits an additional component of O3 at 531.16 eV is associated with the O^{2-} ions in oxygen-deficient regions within the TiO_2 matrix.[40] Moreover, the absence of any signal of Cl as an element or relative derivates in the survey spectrum (Figure 4a) indicates the nanorods are free of NaCl and its derivatives.

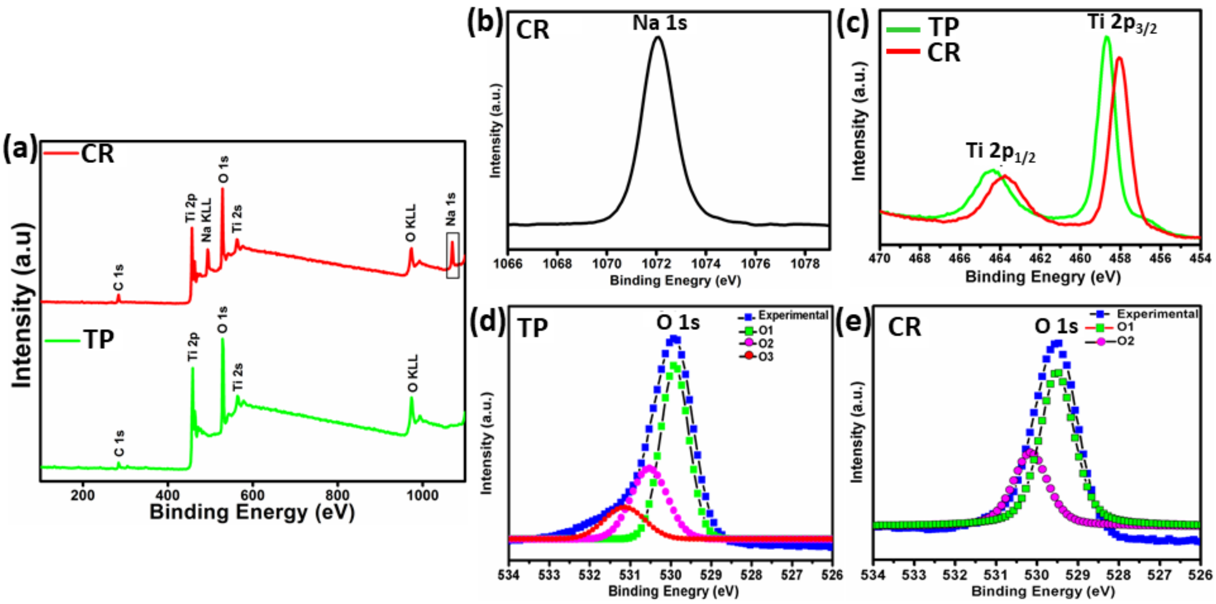

Figure 4. XPS (a) survey, core level spectra of (b) Na-spectrum of CR sample, (c) Ti spectrum of TP and CR sample, respectively, corresponding deconvoluted O 1s spectrum of (d) TP and (e) CR samples.

2.8. Optical and Structural Analysis

UV-Vis absorption spectra of TP sample exhibit a broad absorption ~348 nm, whereas a bathochromic shift (362nm) was observed in the case of CR absorption shown in Figure 6a. The corresponding band gap was calculated using Taucs' equation, and it was found to be ~3.21 and 3.01 eV for TP and CR (shown in Figure S6), respectively. The indirect bandgap value of CR (3.01 eV) falls between the reported band gap values of $Na_{0.23}TiO_2$ phase, which could be suitable as a photoanode material candidate in DSSCs. Figure 5b exhibits a relatively higher reflectance spectrum of the CR attributed mainly due to the random orientation of rod structures than TP. The average thickness of the CR based photoanode film was around 9.42 μm as evident from the FESEM microstructural image, as shown in the inset of Figure 6b.

2.9. Surface Area and Dye Loading Property

In order to unravel the distinction in morphology and photovoltaic performance, the BET surface area of TP and CR samples were measured by nitrogen isothermal adsorption process (Figure 5c). The corresponding pore size was calculated by the BJH method, as shown in the inset of Figure 5c. As evident from Figure 5c, the type *IV* isotherm was observed for both the morphologies. The CR exhibited an enhanced BET specific surface area of 90.03 $m^2.g^{-1}$ than the TP (56.65 $m^2.g^{-1}$), mainly attributed to the thinner rod-based structure. Also, in case of TP sample, a well-defined hysteresis loop indicates the well-developed mesoporous characteristics with an average pore size of ~6 nm. Whereas, the pore size for nanorods was > 50 nm mainly originated from the interlayer space of nanorods, as shown in the inset of Figure 5c. The UV-Vis absorption spectra of the residual dye solution collected after 24 h adsorption on the different morphology of TiO_2 surface was measured by the dye desorption method as shown in Figure 5d. The reduction in the characteristics intensity of the residual N719 dye solution at ~384 and 525 was more for CR than TP sample, which is an indirect evidence for a higher amount of dye adsorbed by CR sample. The higher interlayer space and surface area of the CR sample could have favoured a higher dye loading for the CR sample.

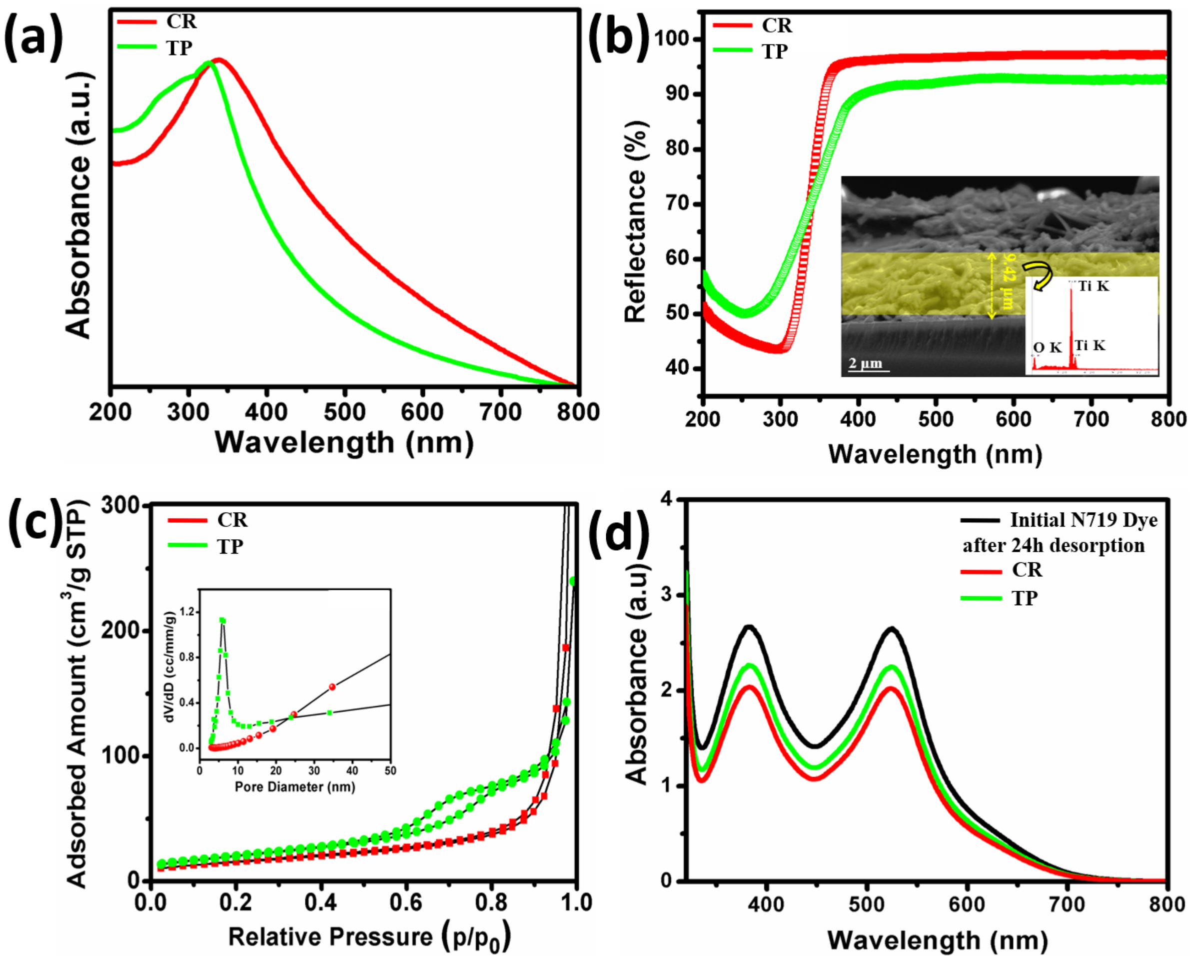

Figure 5. (a) UV-Vis absorption spectra (b) diffuse reflection spectra of TP and CR based films (at inset: cross-sectional FESEM image of the CR based film and corresponding EDX spectrum), respectively, (c) Nitrogen adsorption-desorption isotherm of TP and CR samples, corresponding BJH pore size distribution curves are shown in the inset, respectively and (d) UV-Vis absorption spectra of initial N719 dye and remaining N719 dye after adsorption on TP and CR based photoanode films, respectively.

2.10. Photovoltaic Performance and Electrochemical Impedance Spectroscopy Analysis

In order to evaluate the photovoltaic performance of the synthesized composite rods with the starting precursor TiO_2 and also a standard P25 TiO_2 sample, DSSC devices have been fabricated as per our previous methods.[27,11] The measured performance of the fabricated DSSC device is shown in Figure 6. The *J*-*V* characteristic of the DSSCs fabricated with synthesized CR, TP and P25 are presented in Figure 6a. The fabricated DSSC with CR exhibited a PCE of 7.85% with a short circuit current (J_{SC}) of 16.82 mA.cm^{-2}, open-circuit voltage (V_{OC}) of 0.75 V and a fill factor (FF) of 0.66. On the contrary, TP exhibited a PCE of 3.25% with a short circuit current (J_{SC}) of 8.77 mA.cm^{-2}, open-circuit voltage (V_{OC}) of 0.71 V and FF of 0.53. The details of the device testing parameters for individual tested cells are shown in Table S2.

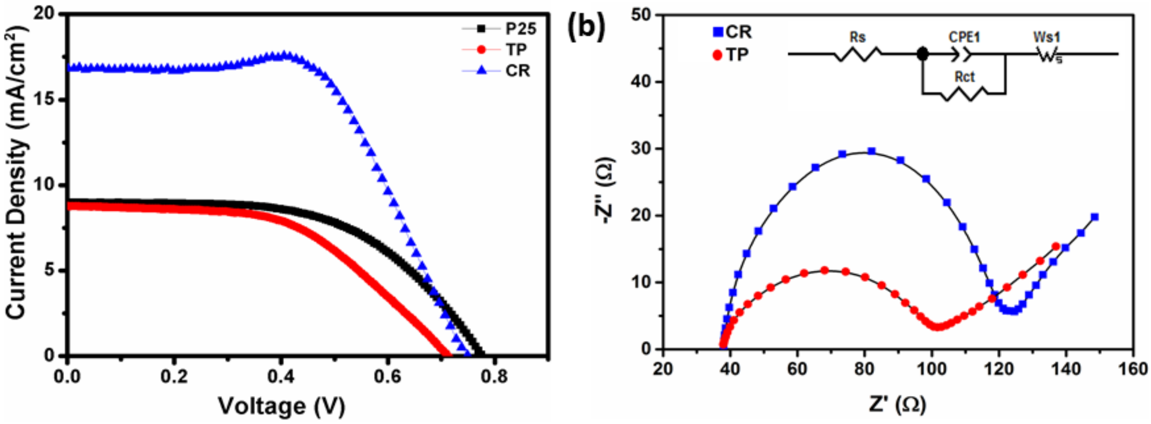

Figure 6. (a) Current density (*J*)-Voltage (*V*) curve of DSSCs fabricated with P25, TP and CR samples, respectively, (b) Nyquist plots of TP and CR based DSSC devices (inset: corresponding equivalent circuit diagram).

We have also compared the photovoltaic performance of P25 nanoparticles which exhibited an efficiency of 3.95% only with an enhanced V_{OC} (0.77 V) and FF (0.56) than the starting TiO_2 samples under identical conditions. The higher efficiency of CR without any surface modification such as applying a scattering layer, or $TiCl_4$ treatment reflects the influence of the CR structure compared to TP and P25 NP.

The electrochemical impedance spectroscopy (EIS) measurements were carried out to understand the transport properties at different interfaces in the DSSC assembly, as shown in Figure 6b. On illumination under 1 SUN, the CR based device exhibited a series resistance (R_S) of 37.92 Ω.cm^{-2} and an electrochemical charge transfer resistance (R_{CT}) of 68.02 Ω.cm^{-2}

whereas the TP based device exhibited an R_S of 37.96 and R_{CT} 78.96 $\Omega.cm^{-2}$, respectively. Interestingly, the R_s value found almost the same for both the devices. However, the $TiO_2/Na_{0.23}TiO_2$ co-existed phase dominates over to particle-based TiO_2 anatase phase device, exhibiting a smaller R_{CT} value, which in turn promotes the transfer of more electrons from the external circuit as evident from the IPCE measurements. The measured parameters are summarized in Table S2.

2.11. Incident Photon-To-Current Efficiency (IPCE) and Cyclic Voltammetry Analysis

The IPCE curve for the N719 dye-sensitized devices exhibited a broad peak over the range of 300-700 nm with a maximum value of ~62 % at 540 nm for the CR based device and ~46 % for TP based device, as shown in Figure 7a. In order to check the cycling ability of the composite photoanode, the cyclic voltammetric (CV) curves were recorded for the champion CR cell, with different numbers of CV cycles, in the voltage window of -1.0 to +1.0 V with a scan rate of 0.05 $mV.s^{-1}$. A typical voltammogram of different cycles executed for a CR film is presented in Figure 7b. Both the anodic and cathodic current simultaneously varies as the number of cycles from 5 to 25. With increasing the testing cycle, current responses are increased and reach a maximum with 20 cycles. The peak currents are dropped with 25 cycles. Moreover, all the cycles trending the voltammogram with similar pattern and narrower peak-to-peak separation, indicating higher electron transfer kinetics, which would enhance the performance of the cell. These results are further adequate agreement with *J-V* result.

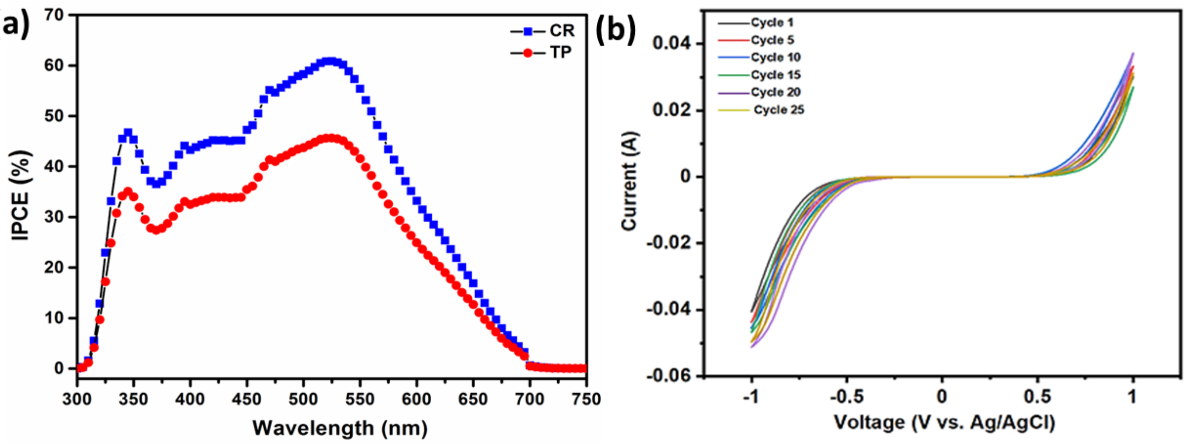

Figure 7. (a) IPCE measurements of TP and CR based DSSC devices, (b) Cyclic voltammogram of CR for different numbers of CV cycles.

In comparison to the reported results on the performance of TiO_2 nanorod based photoanodes in DSSCs, the performance of CR is quite competitive and promising, as shown in Table S3. Consisting of a high V_{OC} of >0.7 V facilitates $TiO_2/Na_{0.23}TiO_2$ nanorods to establish as a potential and new-form of a photoanode candidate for DSSCs.

Interestingly, in this study, the nanorods are formed as the co-existed phase of anatase $TiO_2/Na_{0.23}TiO_2$ in a single morphology, thereby exhibited a higher efficiency compared to TiO_2 nanoparticles and P25 nanoparticles.

We propose that the mixed-phase formation could facilitate faster electron mobilization resulting in better photovoltaic performance, as shown in Figure 8. We believe that the electrons generated in dye-sensitized nanorods migrate first to the anatase phase followed by the titanate phase in the composite and finally to the external FTO.

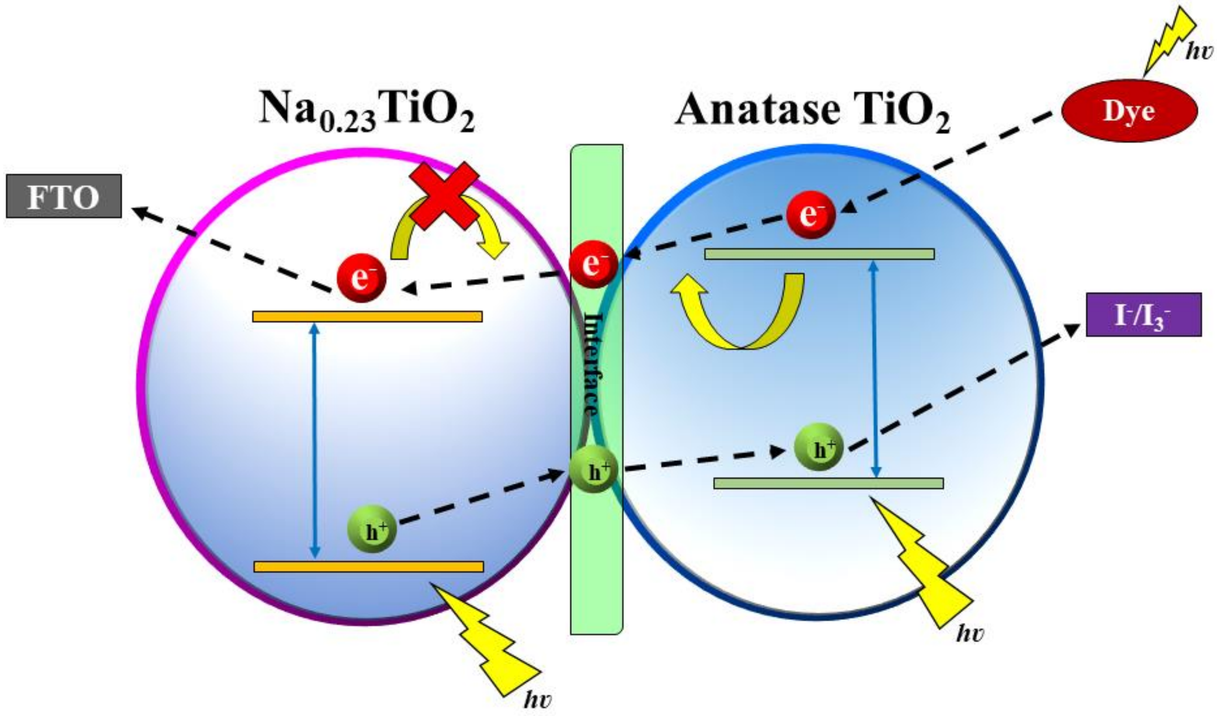

Figure 8. Schematic description of the proposed electron transfer processes and energy band structures of the composite phase and anatase.

Due to the very close bandgap of the two phases, the excited electrons generated in the anatase TiO_2 phase may swiftly migrate towards the CB of the titanate phase in the composite on illumination. Both transferred electrons from anatase TiO_2 and electrons directly excited to the CB of the titanate phase can supply more free electrons to FTO.[48-50]

Furthermore, the rods are expected to facilitate direct conduction pathway with lesser grain boundaries for rapid electron transport than other morphologies as observed in our earlier publications.[51,52] As evident from the microstructure analysis and the diffuse reflection spectra in Figure 6b, the slanting rods in the current case could favour adequate light scattering property and rapid electron transfer both could be responsible for the enhanced light-harvesting to enhance the cell efficiency.[27,53,54] The particles, on the other hand, suffer from trapping/de-trapping phenomenon in the conduction pathway between the grain boundaries and therefore result in lesser efficiency than a rod. However, the low surface area of 1D nanostructures hinders significant improvement of the photovoltaic performance owing to less dye loading compared to nanoparticles. For better balancing of those factors, the inclusion of a composite in a single morphology will be benefited to produce higher efficiency. The enhanced photovoltaic performance of the composite may also arise from the bandgap position of the mixture of phases. Therefore, the observed preliminary result of the device performances based on the synthesized anatase/$Na_{0.23}TiO_2$ co-existed nanorods indicates the advantage of the existence of $Na_{0.23}TiO_2$ phase in enhancing the performance of anatase TiO_2.

2.12. Acetone Sensor Application

As an initiative to eventually develop DSSC powered gas sensor, we have also utilized the synthesized powder for gas sensor fabrication. As a preliminary drive to develop the self-powered gas sensor, we have also utilized the synthesized powder for gas sensor fabrication. An attempt has been taken with the sensor fabricated using the synthesized composite nanorod (CR) powder for the detection of acetone which is considered as the biomarker to detect blood glucose level from breath non-invasively. The acetone concentration for diabetic patients in breath lies in the range from 1.7 ppm to 3.7 ppm, whereas for a healthy person, the concentration range should be below 1 ppm.[55,56] After fabrication of the sensor with CR, the change of resistance was monitored at different acetone concentrations. The sensor was exposed to 10, 5, 3, 2 and 1 ppm acetone at room temperature. The CR based sensor exhibited the response (R_g/R_a) signal as 7.1, 4.7, 4.1, 3.8 and 3.6 for 10, 5, 3, 2 and 1 ppm acetone respectively, at room temperature with 15 sec of exposure time, as shown in Figure 9a. The dynamic response curve of the sensor towards 10, 3 and 1 ppm acetone is presented in Figure 9(b-d). The single cycle of the dynamic response curve of the CR-based sensor for 3 ppm of acetone showing the response and recovery time as 12 sec and 20 sec, respectively, as shown in Figure 9c. Besides, the CR-based gas sensor exhibits enhanced acetone response compared to CO, ethanol and nitrogen gases, which are considered as the interfering gases, as shown in Figure 9e.

Along with the direct current (DC) measurements, we have also used the alternating current (AC) method by using a precision impedance analyzer in the 100 Hz to 1 MHz frequency range to understand the conduction process and the sensing mechanism where Z' indicates the real part and Z" represents the imaginary part of the complex impedance data. The variation of Nyquist diagram of CR based sensor is presented in Figure 9f in presence of air and acetone at room temperature. An attempt has been executed to understand the sensing response with TP-based sensor. However, it showed meagre sensing response (R_g/R_a) about 1.2 towards 10 ppm acetone at 350^{o}C operating temperature.

Interestingly the composite exhibited a p-type sensing behavior compared to TiO_2, which is an n-type semiconducting material. However, further studies are in progress to understand the acetone sensing behavior of the composite powder.

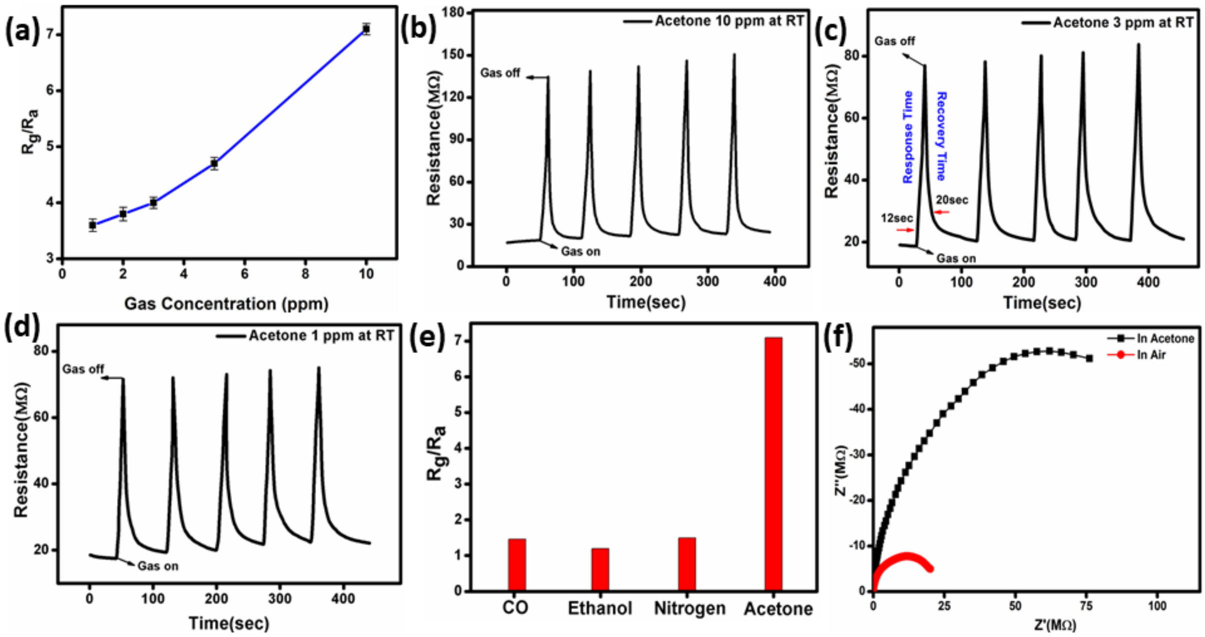

Figure 9. (a) The response of the sensor towards different concentrations of acetone at room temperature (b) dynamic response curve towards 10 ppm (c) 3 ppm, (d) 1 ppm acetone, respectively, (e) selectivity of CR-based sensor towards different gases (f) Nyquist plot of CR-based sensor in air and in presence of acetone.

3. Conclusions

Anatase TiO_2 with $Na_{0.23}TiO_2$ nanorod was synthesized by hydrothermal treatment of the commercially available anatase TiO_2 nanoparticle with NaOH solution at pH 12. It was possible to establish the crucial role of NaOH to obtain the composite phase with interesting nanorod morphology. The TEM study reveals an average diameter of the synthesized nanorod as ~10 nm with an aspect ratio of 25:1 having a BET specific surface area of ~90 $m^2.g^{-1}$. The mixed-phase sample exhibited higher dye loading capacity than the pure anatase sample for DSSC application. Further, the composite phase sample exhibited an enhanced photon to the current conversion efficiency of 7.85% as compared to the precursor pure anatase sample (3.25%). The increased performance of composite nanorod based DSSCs was attributed to the high activity and surface area for increased dye adsorption along with the aligned rod shape for faster electron mobility and light scattering property. Besides, our studies could pave a way to future advancements in the area of DSSCs using less explored composite phase as photoanode. An enhanced p-type semiconducting sensing response was achieved for different concentrations of acetone (10, 5, 2, 3 and 1 ppm) followed by strong selectivity and reproducibility towards acetone at room temperature. The experimental results thus indicate that this simple and cost-effective synthesis process can be used as a promising tool for integrated DSSC powered sensor developments for futuristic application.

4. Experimental Section

Synthesis of composite nanorods: The nanorods were formed under extreme basic condition by a hydrothermal treatment. In detail, 2 g commercial anatase TiO_2 powder (J.T Baker Chemical Co., Baker Analyzed Reagent 1-4162, USA) was mixed with 10 g of NaOH (Merck, Germany) and 25 ml of de-ionized water at a pH of 12 under constant stirring for 2 h and transferred into a 50 mL Teflon lined autoclave kept at 180^{o}C for 48 h. The pH of the synthesis was also varied, keeping other conditions the same. The as-prepared white product was centrifuged at 10,000 rpm and washed with 0.1M HCl (Merck, Germany) to reduce the solution pH ~7. After that, the product was thoroughly washed with de-ionized water. A part of the washed sample was again dissolved in de-ionized water and further treated with 0.1M aqueous $AgNO_3$ solution, where no white precipitate was formed indicating the absence of chloride ion as NaCl form in the sample solution. Finally, NaCl free collected product was dried under the IR lamp at ~80^{o}C (considered as-prepared sample) and then annealed at 500^{o}C in the air for 2 h to convert into the final product (CR sample). 2 g of commercial anatase TiO_2 nanoparticles (TP) was converted to 1.87g of a mixed phase of anatase TiO_2 and $Na_{0.23}TiO_2$ composite nanorods (CR). The same synthesis process has been carried out for different pH (8, 10 and 14) by varying the amount of NaOH (Table S4) only in controlling the morphology. To further perceive the effect of the hydrothermal treatment period, the reaction time has also been varied from 24 h to 48 h in case of pH 12 condition. A detailed amount of various precursors and synthesis parameters for the hydrothermal reaction in controlling the morphology has been described in Table S4.

Material characterization: Thermo-gravimetric analysis (TGA) and differential thermal analysis (DTA) of the as-synthesized sample was carried out from room temperature to 550°C with a heating rate of 10°C.min^{-1} on a NETZSCH 449C simultaneous thermal analyzer to understand the thermal decomposition nature. Structural properties of the as-prepared and calcined powders were characterized by X-ray diffraction method on an X'pert pro MPD XRD of PAN analytical system with CuKα radiation (λ = 1.5406 Å). The optical property of the composite sample and its dye (N719) loading capability was measured by a UV-Vis-NIR spectrophotometer (Shimadzu, UV-3600). The morphology of the precursor, as-prepared and calcined samples, was monitored through a field emission scanning electron microscope (FESEM), (LEO 430i, Carl Zeiss) and a high-resolution transmission electron microscope operating at 300 kV (Tecnai G2 30ST, FEI). The surface charge analysis (zeta potential) of the sample has been measured using a Horiba Nanoparticle Analyzer SZ100. Besides, the X-ray photoelectron spectroscopy (XPS) measurements were carried out by a PHI 5000 Versa probe II scanning XPS microprobe (ULVAC-PHI, U.S.). BET (Brunauer, Emmett and Teller) specific surface area of a sample is measured using a Quantachrome (iQ3) instrument after evacuation at 150°C for 4 h including the BJH (Barrett, Joyner, and Halenda) pore size distribution. Thickness measurement and energy dispersive X-ray elemental analysis (EDX) of fabricated nanorod film was performed in the same instrument used for FESEM. The diffuse reflectance (DR) spectrum of the films is measured using UV-Vis-NIR spectrophotometer (Shimadzu, UV-3600).[11,45]

Fabrication of DSSC: The photoanode films having an area of 0.2826 cm^2 were fabricated by a screen printing (120T mesh/inch, Mascoprint, UK) method on fluorine-doped tin oxide (FTO) (7 $\Omega.cm^{-2}$) glass substrate using a homemade paste made with ethyl cellulose and α-terpinol (Sigma Aldirch). The coated films were annealed in an oven at 450°C for 30 min. The prepared photoanode films were soaked in an N719 dye (0.5 mM, Solaronix) with absolute ethanol (Merck, Germany) at room temperatures for 24 h for the dye adsorption on the film. After dye adsorption, the prepared films were thoroughly washed with absolute ethanol for removing the excess dye molecules present at the surface of the film. Pt solution (Platisol T, BN 40/170311FM, Solaronix, Switzerland) having Pt particles in size range of 10-20 nm were dropped cast on a cleaned FTO glass. The deposited layer was gradually dried in air and then heated at 450°C for 15 min, in order to activate the platinum layer for working. Finally, the prepared I_3^-/I^- liquid electrolyte was infiltrated into the photoanode cell, and a sandwiched DSSC device with the Pt counter electrode was fabricated. The dye adsorbed TiO_2, and Pt-FTO glass was merged like sandwich-type with a hot-melt film (~25 μm, Surlyn, Dyesol) between them. The photovoltaic performance of the prepared sandwich-type devices was measured under 1000$W.m^{-2}$ light from a Wacom AAA continuous solar simulator (model: WXS-210S-20, AM1.5G. The *I-V* characteristic study has been carried by using an EKO MP-160i *I-V* Tracer.[11,27] All the data represented are an average of measurements taken on five different devices for both the TiO_2 samples. Electrochemical impedance spectroscopy (EIS) measurements were performed with an Autolab frequency analyzer setup equipped with an Auto lab PGSTAT 10 and a frequency response analyzer (FRA) module under solar simulator condition with the frequency range from 0.1 Hz to 100 kHz and at the 0.70 V open-circuit voltage of the devices. The cyclic voltammetry analysis was carried out in a three-electrode assembly cell comprising of the composite film as the working electrode, Ag/AgCl as reference electrode and platinum as the counter electrode in the presence of I^-/I_3^- electrolyte using the NOVA software equipped with the Autolab potentiostat/galvanostat instrument. Besides, the incident photon to current efficiency (IPCE) was measured on a Bentham PVE300 Photovoltaic EQE (IPCE) under 300-800 nm wavelength range.

Fabrication of gas sensor and measurements: The synthesized powder samples are used for sensor fabrication. At first, a certain amount of powder sample was ground smoothly in a motor pestle with isopropyl alcohol to make a paste. Sensor fabrication and details are reported elsewhere.[57,58] After making a coating of the paste on the alumina substrate, it was dried at 80^{o}C. When the fabricated sensor element was exposed to acetone, the resistance of the sample changed, and the response was calculated from the change in resistance at room temperature. The response level was measured towards various concentration levels of acetone, and sensitivity percentage (S) was calculated as the ratio of R_g/R_a where the electrical resistances are denoted as R_g and R_a in the presence of acetone and air, respectively. The electrical measurements were performed by using an Agilent multimeter (Model No. U1253A). The AC measurements have been carried out on a precision impedance analyzer (6500 B Wayne Kerr) within a wide range of frequency from 100 Hz to 1 MHz.

Supporting Information

The TG-DTA analysis of the as-prepared sample after hydrothermal treatment of commercial anatase TiO_2 and NaOH at a pH of 12. XRD pattern and EDX analysis of (a) powder sample just prepared and collected after the hydrothermal reaction, and before HCl wash (pH 12), (b) after HCl wash (pH 7) and (c) followed by a wash with de-ionized water (pH 7), respectively, Colour elemental mapping, and quantitative EDX analysis plot of CR sample. Raman spectra of the precursor and final sample. Band gap calculation from Tauc's plot. Table of XPS binding energies of TP and CR samples. Table of Photovoltaic, impedance spectroscopic parameters and incident photon-to-current efficiency (IPCE) obtained for CR and TP devices, respectively. Table for Comparison of the device parameter of $TiO_2/Na_{0.23}TiO_2$ nanorods with different TiO_2 phases and their morphology in a DSSC device. Table for amount calculation of various precursors and synthesis parameters for the hydrothermal reaction.

Acknowledgements

PG gratefully acknowledges INSPIRE program of the Department of Science and Technology (DST), Govt. of India for the PhD fellowships. AR acknowledges Newton-Bhabha Fellowship Program 2016-2017 funded by DST, Govt. of India and the British Council. The authors acknowledge the help rendered by Dr. Jiten Ghosh, Principal Scientist, Advanced Mechanical and Material Characterization Division, CSIR-Central Glass and Ceramic Research Institute, Jadavpur, Kolkata 700032, for the XRD analysis.

Conflict of Interest

The authors declare no conflict of interest.

Keywords

Hydrothermal, Sodium Titanate, Nanorod, Photovoltaic, Acetone sensor

[1] H. Zhang, J. F. Banfield, *Chem. Rev.* **2014**, *114*, 9613.

[2] R. Verma, J. Gangwar, A. K. Srivastava, *RSC Adv.* **2017**, *7*, 44199.

[3] F. D. Angelis, C. D. Valentin, S. Fantacci, A. Vittadini, A. Selloni, *Chem. Rev.* **2014**, *114*, 9708.

[4] S. D. Mo, W. Y. Ching, *Phys. Rev. B* **1995**, *51*, 13023.

[5] D. A. H. Hanaor, C. C. Sorrell, *J. Mater. Sci.* **2011**, *46*, 855.

[6] P. Selvaraj, A. Roy, H. Ullah, P. S. Devi, A. A. Tahir, T. K. Mallick, S. Sundaram, *Int. J. Energy Res.* **2019**, *43*, 523.

[7] B. Liu, E. S. Aydil, *J. Am. Chem. Soc.* **2009**, *131*, 3985.

[8] N.-G. Park, J. van de Lagemaat, A. J. Frank, *J. Phys. Chem. B* **2000**, *104*, 8989.

[9] G. Li, C. P. Richter, R. L. Milot, L. Cai, C. A. Schmuttenmaer, R. H. Crabtree, G. W. Brudvig, V. S. Batista, *Dalton Trans.* **2009**, 10078.

[10] J. Tian, Z. Zhao, A. Kumar, R. I. Boughton, H. Liu, *Chem. Soc. Rev.* **2014**, *43*, 6920.

[11] A. Roy, P. P. Das, P. Selvaraj, S. Sundaram, P. S. Devi, *ACS Sustain. Chem. Eng.* **2018**, *6*, 3299.

[12] K. Lee, A. Mazare, P. Schmuki, *Chem. Rev*. **2014**, *114*, 9385.

[13] Y. Bai, I. Mora-Sero, F. D. Angelis, J. Bisquert, P. Wang, *Chem. Rev.***2014**, *114*, 10095.

[14] T. Sagawa, S. Yoshikawa, H. Imahori, *J. Phys. Chem. Lett.* **2010**, *1*, 1020.

[15] S. Mukhopadhyay, D. Maiti, A. Saha, P. S. Devi, *Cryst. Growth Des.* **2016**, *16*, 6922.

[16] P. I. Gouma, M. J. Mills, *J. Am. Ceram. Soc.* **2001**, *84*, 619.

[17] M. Evain, M. H. Whangbo, L. Brohan, R. Marchand, *Inorg. Chem.***1990**, *29*, 1413.

[18] Z. Q. Guo, J. P. Zhou, L. L. An, J. X. Jiang, G. Q. Zhu, C. Y. Deng, *J. Mater. Chem. A* **2014**, *2*, 20358.

[19] J. Z. Wang, J. P. Zhou, Z. Q. Guo, Y. X. Lei, Q. U. Hassan, *Cryst. Res. Technol.* **2018**, *53*, 1700153.

[20] J. Huanga, R. Meng, L. Zua, Z. Wang, N. Feng, Z. Yang, Y. Yu, J. Yang, *Nano Energy* **2018**, *46*, 20.

[21] D. Morais da Silva, B. S. Canuto de Menezes, V. D. N. Bezzon, T. L. A. Montanheiro, E. F. Macedo, D. B. Tada, G. Petraconi, G. P. Thim, *SN Applied Sciences* **2019**, *1*, 945.

[22] A. Fujishima, T. N. Rao, *Proc. Indian Acad. Sci.* **1997**, *109*, 471.

[23] Y. Paz, A. Heller, *J. Mater. Res.* **1997**, *12*, 2759.

[24] X. Wu, G. M. Lu, L. Wang, *J. Colloid Interface Sci.* **2013**, *391*, 70.

[25] S. Shalini, R. Balasundaraprabhu, T. S. Kumar, N. Muthukumarasamy, S. Prasanna, K. Sivakumaran, M. D. Kannan, *Mater. Lett*. **2018**, *221*, 192.

[26] S. Mukhopadhyay, D. Maiti, S. Chatterjee, P. Sujatha Devi and G. S. Kumar, *Phys. Chem. Chem. Phys.*, **2016**, 18, 31622-31633.

[27] A. Roy, S. Mukhopadhyay, P. Sujatha Devi, S. Sundaram, *ACS Omega* **2019**, *4*, 1130.

[28] B. Fan, Y. Zhang, R. Yan, J. Fan, *Cryst. Eng. Comm.* **2016**, *18*, 6492.

[29] M. Lin, Z. Y. Fu, H. R. Tan, J. P. Y. Tan, S. C. Ng, E. Teo, *Cryst. Growth Des.* **2012**, *12*, 3296.

[30] Y. V. Kolen'ko, K. A. Kovnir, A. I. Gavrilov, A. V. Garshev, J. Frantti, O. I. Lebedev, B. R. Churagulov, G. Van Tendeloo, M. Yoshimura, *J. Phys. Chem. B* **2006**, *110*, 4030.

[31] J. NoéDíaz de León, J. R. Rodríguez, J. Rojas, Y. E. Barrón, L. Cardenas, C. R. Kumar, G. A. Nuñez, S. F. Moyado, *Front. Chem.* **2019**, *7*, 750.

[32] C. C. Tsai, H. Teng, *Chem. Mater.* **2006**, *18*, 367.

[33] S. Shalini, N. Prabavathy, R. Balasundaraprabhu, T. S. Kumar, P. Walke, S. Prasanna, D. Velayuthapillai, *J Mater Sci: Mater Electron.* **2017**, *28*, 3500.

[34] V. M. Ramakrishnan, N. Muthukumarasamy, P. Balraju, S. Pitchaiya, D. Velauthapillai, A. Pugazhendhi, *Int. J. Hydrog. Energy*, **2020**, *45*, 15441.

[35] L. Lan, Z. Yichao, L. Yanzhong, Z. Kaiqiang, H. Jinxian, H. Zhigao, M. Sanjay, H. Zhensheng, *Nanoscale*, **2020**, *12*, 230.

[36] J. Y. Eom, S. J. Lim, S. M. Lee, W. H. Ryu, H. S. Kwon, *J. Mater. Chem. A* **2015**, *3*, 11183.

[37] M-N. Li, Z-Y. Chi, Y-C. Yu, *J. Am. Ceram. Soc.* **2012**, *95*, 3297.

[38] D. Nassoko, Y. F. Li, J. L. Li, X.Li, Y. Yu, *Int. J. Photoenergy* **2012**, 1.

[39] I. Singh, B. Birajdar, *RSC Adv.* **2017**, *7*, 54053.

[40] A. Sinhamahapatra, J-P. Jeon, J-S. Yu, *Energy Environ. Sci.* **2015**, *8*, 3539.

[41] Y. Dong, K. Pan, G. Tian, W, Zhou, Q. Pan, T. Xie, D. Wang, H. Fu, *Dalton Trans*. **2011**, *40*, 3808.

[42] L. Qi, C. Li, Y. Chen, *Chem. Phys. Lett.* **2012**, *539*, 128–132

[43] J.-Y. Liao, J.-W. He, H. Xu, D.-B. Kuang, C.-Y. Su, *J. Mater. Chem.* **2012**, *22*, 7910.

[44] T. Peng, J. Xu, R. Chen, *Chem. Phys. Lett.* **2020**, *738*, 136902.

[45] P. P. Das, A. Roy, S. Das, P. S. Devi, *Phys. Chem. Chem. Phys*. **2016**, *18*, 1429.

[46] L. Wei, P. Wang, Y. Yang, R. Fan, Y. Yang, Y. Qiu, *Sustain. Energy Fuels*, **2017**, *1*, 1112.

[47] A. Latin, C. Cavallo, F. K. Aldibaja, D. Gozzi, *J Phys. Chem. C* **2013**, *117*, 25276.

[48] G. Yang, H. Ding, J. Feng, Q. Hao, S. Sun, W. Ao, D. Chen, *Sci. Rep.* **2017**, *7,* 14594.

[49] D. Yang, H. Liu, Z. Zheng, Y. Yuan, J. Zhao, E. R. Waclawik, X. Ke, H. Zhu, *J. Am. Chem. Soc.* **2009**, *131*, 17885.

[50] Y. Chimupala, P. Junploy, T. Hardcastle, A. Westwood, A. Scott, B. Johnson, R. Brydson, *J. Mater. Chem. A* **2016**, *4*, 5685.

[51] P. P. Das, S. A. Agarkar, S. Mukhopadhyay, U. Manju, S. B. Ogale, P. S. Devi, *Inorg. Chem.* **2014**, *53*, 3961.

[52] A. Roy, P. P. Das, M. Tathavadekar, S. Das, P. S. Devi, *Beilstein J. Nanotechnol*. **2017**, *8*, 210.

[53] M. Ge, C. Cao, J. Huang, S. Li, Z. Chen, K. Q. Zhang, S. S. Al-Deyab, Y. Lai, *J. Mater. Chem. A* **2016**, *4*, 6772.

[54] P. Mazzolini, T. Acartürk, D. Chrastina, U. Starke, C. S. Casari, G. Gregori, A. L. Bassi, *Adv. Electron. Mater.* **2016**, *2*, 1500316.

[55] A. Staerz, U. Weimar, N. Barsan, *Sensor*, **2016**, *16*, 1815.

[56] N. Zhang, S. Ruan, Y. Yin, S. Wen, Y. Chen, *ACS Appl. Nano Mater.* **2018**, *1*, 4671.

[57] P. Nag, S. Banerjee, Y. Lee, A.Bumajdad, Y. Lee, P. S. Devi, *Inorg. Chem.***2012**, *51*, 844.

[58] P. Nag, S. Majumdar, A. Bumajdad, P. S. Devi, *RSC Adv.***2014**, *4*, 18512.

For Table of Contents Only